Turbulent Combustion Data Analysis Using Fractals

Warren C. Strahle*
Georgia Institute of Technology, Atlanta, Georgia 30332

This paper investigates several types of data analysis, based upon fractal geometry concepts, using time series generated in turbulent combustion research. The techniques are quite general and may be used for other turbulent flows. Investigated are the generalized fractal dimension, multifractal probability density function, fractal filtration, multifractal spectrum, and fractal interpolation and its possible connection with chaotic dynamics. It is concluded that several of the techniques are useful for 1) new visual depiction of the data, 2) discrimination of portions of data traces as noise-contaminated, 3) separation of wanted and unwanted high- or low-frequency events, and 4) interpolation between sparse data points in either short run time or low data acquisition rate situations.

Introduction

TIME series or instantaneous space distributions obtained from turbulent combustion data analysis are rich in complexity. There are simply more physical phenomena occurring in such flowfields than in those of constant-density, fixed-composition fields as in incompressible turbulence. Since fractal geometry has found its uses in describing field quantities in constant density turbulence, such as in Refs. 1–3, it is reasonable that it should find even greater use in the description of turbulent reacting flows.

Fractal geometry has, in fact, found initial introduction into analysis of turbulent premixed combustion[4,5] and turbulent diffusion flames.[6] Several workers (too numerous to cite here and not particularly relevant to the points that are to be made in this paper) have used the calculation of fractal dimension in their descriptions of experimental results. As a descriptor of the "wiggliness" of some picture, the fractal dimension (to be quantified in more detail later) has become a common quantity to present, in addition to other detail such as spectra and probability density functions (pdf).

Turbulence is a chaotic motion of a fluid for which fractal geometry becomes a natural tool of analysis. In fact, the trend is toward analysis of turbulence as not quite so chaotic (random) as previously thought, but with more determinism in analysis. This has led the author toward application of fractal geometry to time series analysis and filter applications in Refs. 7 and 8. Those works were preliminary in nature and will be expanded upon in this paper.

This paper is concerned with several techniques of fractal geometry application to time series analysis. Turbulent combustion is the vehicle used for generation of the time series, simply because of the author's interests, but the techniques are general. Many of the techniques are contained in an excellent new book[9] on the subject (see the Acknowledgments) and are also drawn from the literature, but some are original to the work here. Specifically, the issues that will be addressed in this paper consist of the following: 1) the generalized dimension, 2) the usual fractal (or capacity or similarity) dimension, 3) the multifractal pdf, 4) signal filtration, 5) the multifractal spectrum, 6) fractal interpolation as a data augmentor, and 7) a possible connection to chaotic dynamics that may explain why some of the techniques work. The subject of hidden variable fractal interpolation will be touched upon briefly.

Received Nov. 6, 1989; revision received Feb. 12, 1990; accepted March 5, 1990.

*Regents' Professor, School of Aerospace Engineering. Fellow AIAA.

Data Sets

Four sets of data are used for analysis: three real and one contrived. Shown in Fig. 1 are these time series, two taken from a turbulent premixed flame, one from a subsonic ramjet combustor simulator, and the last generated by a random number generator. The apparatus used for the first two, the Rayleigh scattering trace and the hot film anemometer trace, is described in Ref. 8. The apparatus used for the Raman scattering trace is described in Ref. 10. The last trace is a train of rectangular pulses with random arrival times with the tops and bottoms contaminated with high-frequency noise of a uniformly distributed pdf with a peak to peak of 10% of the mean peak amplitude.

The most important point concerning these data sets is that the neighboring points of Figs. 1a, 1b, and 1d are close enough to be correlated with one another, whereas the data points on Fig. 1c (the Raman trace) are not. The time series of Fig. 1c was taken by a pulsed laser with a repetition time of 0.2 s, which was far too long for a significant correlation between data points (the correlation coefficient between points was 0.017 for 1024 points used in the calculation). For viewability Fig. 1 has all data points connected by straight lines. The actual points were from digitized data.

The data presented are "wiggly." They are chaotic with broadband power spectra and pdf that are smooth and broad (except for the rectangular pulse train, which has two near-delta functions at the upper and lower mean positions). Actually, the pdf values for both the Rayleigh scattering trace and the rectangular pulse train show bimodal properties reminiscent of, say, a temperature trace that would be seen in a premixed flame of Bray-Moss-Libby (BML) structure.[11] The Raman trace shows near-Gaussian structure as does the hot film trace, more closely resembling a pdf in cold flow turbulence. This information is only presented for the curious reader. From now on, only the fractal geometry of the traces and the uses of fractal geometry in data treatment are of interest.

Although it is also irrelevant for the main purposes of this paper, the interested reader may wish to know the sampling rate of the data in Figs. 1a–1d. Figure 1a was obtained at 100,000 data points per second; Fig 1b was sampled at 30,000 per second; Fig. 1c, because of a pulsed laser, was gained at 5 per second; and Fig. 1d was contrived, with the "hash" at the first peak using 1/50 of the distance between the first two peaks and the same "time" separation for all hash on all peaks and troughs thereafter.

The lines on the piece of paper of Fig. 1 have topological dimension of unity, i.e., $y(t)$ with y the ordinate and t the abscissa is a one-dimensional graph. If one filled in the entire graph with ink to make a black area, the topological dimension would be two, an area. The entire idea of what follows is that the traces are so "wiggly" that they do not have a real

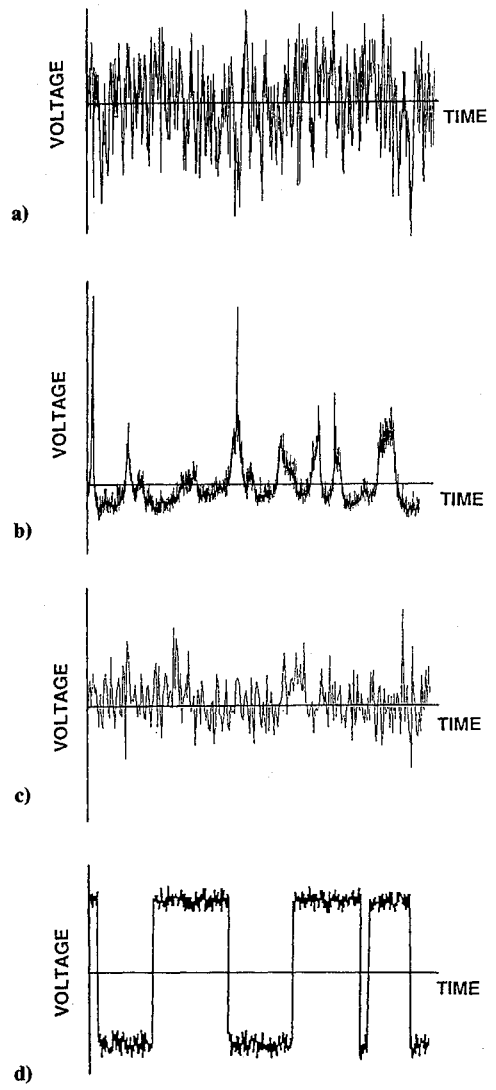

Fig. 1 Four data traces used for analysis: a) measurement from a hot film measurement in a relatively cold portion of a turbulent premixed flame; b) Rayleigh scattering measurement in the hot portion of the same flame; c) Raman spectroscopy measurement in a turbulent diffusion flame in a wind tunnel; and d) contrived waveform using a random number generator.

dimension of unity, but that their apparent dimension lies between one and two.

Analysis

Generalized Dimension

Consider a digitized time series with $N+1$ points with each time point labeled t_i with $i = 0, 1, 2, \ldots, N$. To each t_i there corresponds a value of the ordinate y_i. This is shown by example in Fig. 2a. Consider also that the entire graph is covered by boxes of width and height ε (although not necessary, one may presume that both coordinates have maximum amplitude unity by appropriate normalization). Now throw away all boxes not containing one or more data points. This now yields a total of $M \leqq N$ boxes containing data. Each box may be labeled by an integer m, as shown in Fig. 2a, and the number of data points in each mth box is M_m. One may define a probability p_m that the mth box contains a poin $p_m = M_m/M$. The generalized dimension is then defined by[1]

$$D_q = \lim_{\substack{\varepsilon \to 0 \\ N \to \infty}} \frac{\log(\Sigma_m p_m^q)}{(q-1)\log(\varepsilon)} \qquad (1)$$

In practice a finite data record is available; hence, the limit $N \to \infty$ cannot be taken. Moreover, it is clear the $\varepsilon \to 0$ is meaningless in practice since below some limit each of the m boxes would contain only one point and the numerator of Eq. (1) would no longer change with a change in ε. However, if the derivative of the numerator with respect to $\log(\varepsilon)$ is taken, there results

$$(q-1)D_q = \mathrm{d}\log(\Sigma p_m^q)/\mathrm{d}\log(\varepsilon)$$

That is, a straight line with slope $(q-1)D_q$ should result on a log-log plot if the generalized dimension exists over a range of ε.

What often results in turbulent combustion time series is that, over a range of ε, termed the inner and outer cutoffs, a straight line does occur. This is schematically depicted in Fig. 2b for $q = 0$. This very important q value yields D_0 and is denoted the fractal, capacity, or similarity dimension. For $q = 0$, p_m^q is unity, and the sum in the numerator of Eq. (1) is merely the number of covering boxes, M. In practice, in order to avoid voids between boxes, the data points may be connected by straight lines, and the now continuous curve is covered by boxes that always touch each other. This only works for D_0, however.

An alternative computational procedure, which has been found to yield answers very close to a box counting procedure, is to first pick an ε along the time axis. Second, search the data string between t_i and $t_i + \varepsilon$, finding the maximum and minimum y values in this interval. Approximately (usually very close), the number of boxes, $n_i(\varepsilon)$, in this interval is

$$n_i(\varepsilon) = (y_{\max} - y_{\min})/\varepsilon$$

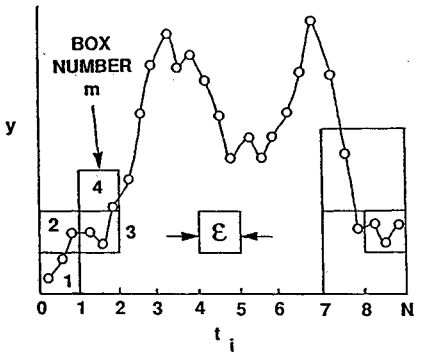

a)

$M_1 = 2 \quad M_2 = 1 \quad \text{etc.}$

$M = \sum_m M_m$

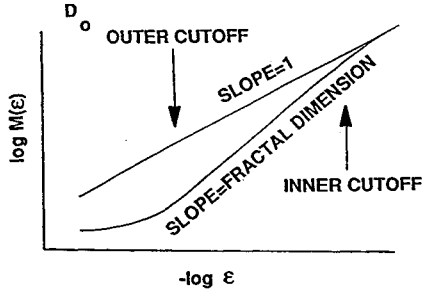

b)

Fig. 2 Curve a illustrates the box counting procedure for calculating probabilities needed for the generalized dimension. Curve b shows a schematic of an expected result for the dimension of order zero (fractal dimension).

and the total number of boxes is obtained by summing over all ε intervals. The error at each i is a fraction of unity in the integer number of boxes that would be exactly calculated.

There are several other definitions and ways of computing dimensions, as may be found, for example, in Ref. 13. For some of the calculations the error bounds have been estimated in Ref. 14. However, in this paper only the methods described earlier have been used.

Fractal Dimension and the Multifractal pdf

The fractal dimension of the curves in Figs. 1a and 1b has previously been reported.[8] The fractal dimension of the curves in Figs. 1c and 1d have been computed by the method given earlier, and the results are compiled here:

$D_0 = 1.58$ (Fig. 1a)

$D_0 = 1.55$ (Fig. 1b)

$D_0 = 1.70$ (Fig. 1c)

$D_0 = 1.45$ (Fig. 1d)

These dimensions reveal the space-filling nature of the curves. Although the first and second traces look quite different and represent different physical phenomena, the blackening of a piece of paper is about the same. The fourth curve is not as space-filling as the first three. The Raman curve, containing mostly uncorrelated points, has a high fractal dimension, suggesting the obvious. Presentation of a single number such as the fractal dimension is not particularly revealing, just as presentation of simply the turbulence intensity leaves out a lot of detail. Most research workers might be more interested in the pdf of turbulence velocities; analogously, the computation of the pdf of fractal dimensions turns out to be very revealing. This pdf will be called the multifractal pdf and measures the distribution of local fractal dimensions. This calculation is described in Ref. 8, but the method is repeated here.

What one is trying to do is to calculate the local slope of log(boxes) with respect to log(ε). First, calculate $n_i(\varepsilon)$ from t_i to $t_i + \varepsilon$. Do it again from $t_i + \varepsilon$ to $t_i + 2\varepsilon$. Start again, but choose an interval of 2ε, and carry out the calculation from t_i to $t_i + 2\varepsilon$. Call the first two n_i, n_1 and n_2 and the last one n_3. The local fractal dimension is

$$D_{0,\text{local}} = [\log(n_3) - \log(n_1 + n_2)]/\log(2)$$

Then construct a pdf of these local results from the total time series. Results of this calculation from 4096 points of the Rayleigh scattering trace are shown in Fig. 3 for various values of ε. At low values of ε the pdf bunches about unity, whereas at high values of ε the pdf gathers about two. But in an intermediate range of ε the pdf is quite stable; it is in this range that the curve has fractal-like behavior with a fractal dimension, on average, of about 1.55.

A quite different picture is presented in Fig. 4 for the Raman scattering trace with an average fractal dimension of about 1.7. This occurs because neighboring points on the Raman scattering trace are uncorrelated with one another. The original time series is largely a space-filling curve.

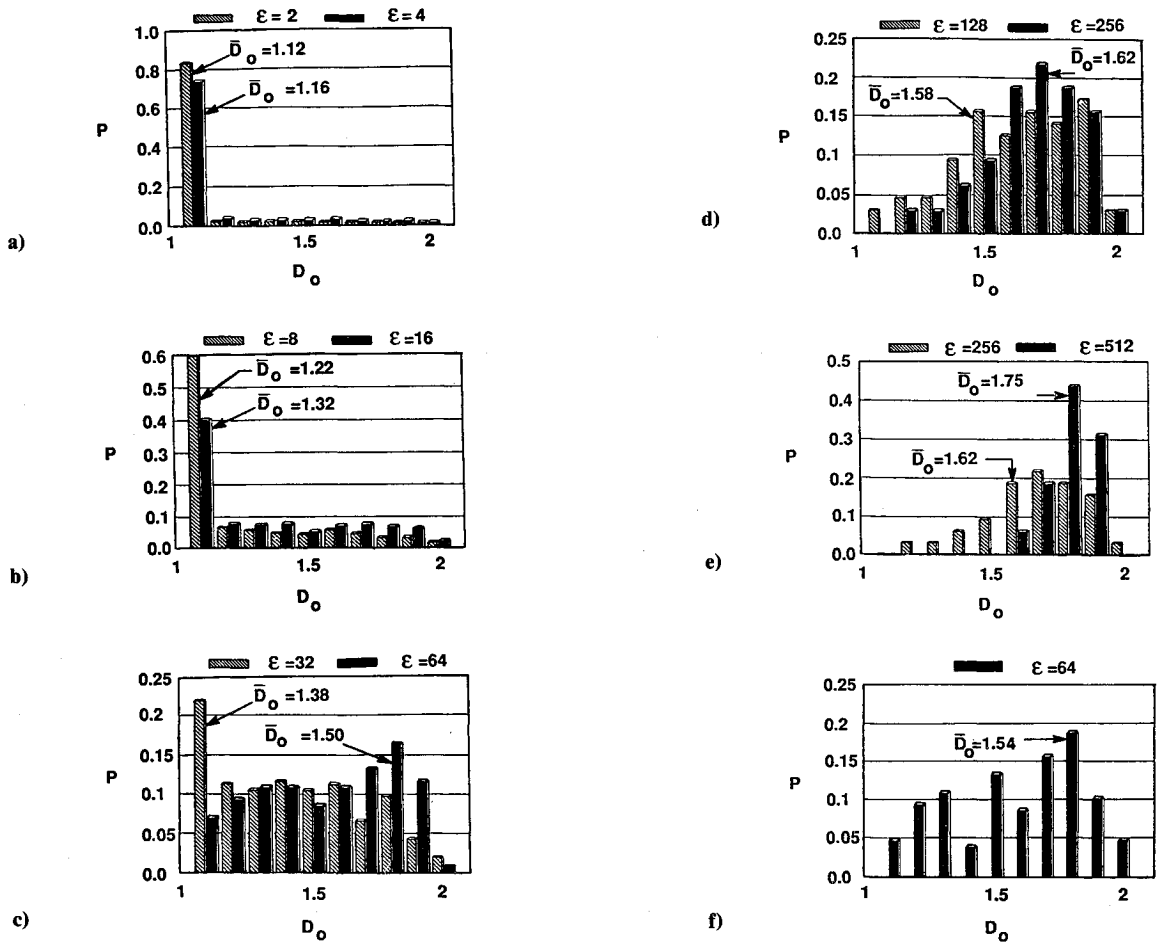

Fig. 3 Multifractal pdf of the Rayleigh trace for various values of the box size. A comparison curve is given at the bottom for a given box size for the hot film trace.

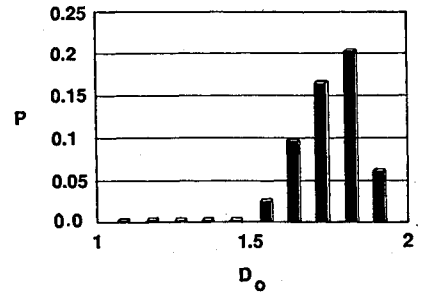

Fig. 4 Multifractal pdf for the Raman trace.

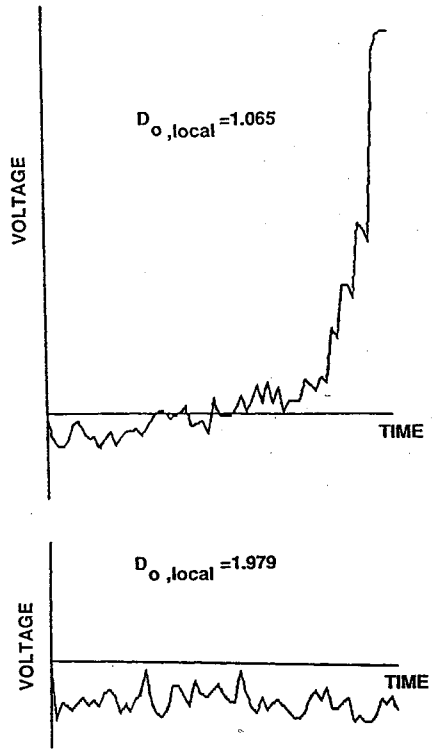

Fig. 5 Two segments of the Rayleigh time series showing radically different local fractal dimensions.

Aside from giving a new pictorial representation of the complexity of the time series, there is a technological use for the local fractal dimension. A local calculation of this dimension is shown for the short segment of the Rayleigh scattering trace in Fig. 5. Notice that in regions of large moves in the time series (the spikes in the trace) the fractal dimension is low, whereas in the noisy parts of the trace (the troughs) the fractal dimension is large. If one were to take a Fourier spectrum of this time series, both the spikes and the noise in the troughs would contribute to the high-frequency portion of the spectrum. However, the local fractal dimension distinguishes between the two types of events. It is known from the physics of the situation that the spikes are real, wanted events (they are cold spots in the turbulent flame), whereas the noise in the troughs is shot noise from the photomultiplier and is unwanted contamination of the data. Therefore, a natural conclusion is that the local fractal dimension may be used as an indicator for signal filtration between different types of high-frequency events.

Fractal Filtration

A common technique for filtering out noise from a time series, in addition to analog filtration of the original signal, is to use some form of digital filtration.[15] But such filtration is not discriminatory with different types of high- (or low-) frequency events. Monitoring of the local fractal dimension provides such discrimination, as has been presented in Ref. 7.

The use of a discriminator along with a linear digital filter creates a nonlinear filter. Any digital filter may be used, but here a simple first-order lag recursive filter will be used as a demonstration. Consider that the trace, chosen here as Fig. 1d, is to be filtered by

$$y_{i,\text{filtered}} = \alpha y_i(t) + (1-\alpha) y_{i-1,\text{filtered}}$$

where the filter parameter is chosen by the user. Using $\alpha = 0.05$ this filter is applied to Fig. 1d, and the results are shown in Fig. 6a. A well-known problem results in that, although it is true that the noise has been removed from the peaks and troughs, the vertical character of the rectangular transitions is lost. Moreover, the narrow trough is completely lost, and in general there is a phase lag introduced with this filter. The filter has shown no discrimination between two types of high-frequency events.

Now consider that 32 points to the left of t_i and 32 points to the right are used to compute the local fractal dimension. The following formula (α linear in D_0) is then applied to pick a local value of the filter parameter α:

$$\alpha = (D_0 - 1.45) * 1.73 + 0.05, \qquad D_0 \geqq 1.45$$

$$\alpha = (D_0 - 1) * 0.111, \qquad D_0 \leqq 1.45$$

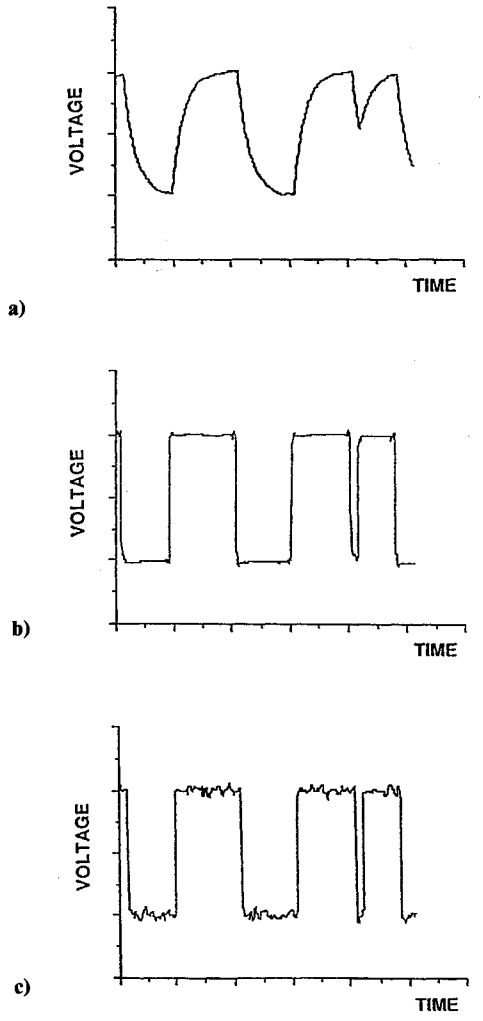

Fig. 6 Three types of digital filtration applied to the trace of Fig. 1d: a) using a first-order lag recursive filter; b) using a fractal filter as a discriminant to the use of filter (a); and c) using a median filter.

This allows no filtration if $D_0 = 1$ and a no-pass condition if $D_0 = 2$. The results are shown in Fig. 6b. It is seen that both the sharp moves are retained, there are no phase lags introduced, and the noise on the peaks and troughs is largely removed.

There are other nonlinear filters designed to cope with the rapid changes of the large moves, e.g., the median filter.[16] If one goes to a given number of points both before and after the central point of issue (in this case 5) and chooses the median value of the y obtained as the filtered point, one can catch the large stepwise moves, as shown in Fig. 6c. However, the median filter does not do as well as the adaptive fractal filter in removing the noise in the tops and troughs.

In the examples given the points chosen for both nonlinear filters were chosen equidistant from the central point of interest. This presumes postprocessing of data. If this is to be done in real time, only data points before the one of interest can be used for processing. This will delay the onset of recognition of a coming low (or high) fractal dimension event (or, in the case of the median filter, a large step). In the case of the fractal filter this would allow some "hash" to appear right after the large step change. As with any filter, the practitioner must adjust the filter parameters and the number of data points used in the discrimination process to achieve the best results. At this time, it is reiterated that the fractal discrimination can be used with any digital filter, and this is also at the choice of the practitioner.

Although there appear several uses for the use of fractal analysis in filtration, perhaps also in the cleaning up of images produced by fractal image compression,[17] it currently appears that it is most useful in discrimination between wanted and unwanted high-frequency events. It has been employed for precisely this problem for the Rayleigh trace of Fig. 1b in Ref. 7, which bears a strong resemblance to the model trace of Fig. 1b in frequency characteristics. Further work is warranted to find applications for such an adaptive filter.

Multifractal Spectrum

Just as the multifractal pdf gives information about the distribution of D_0 along a time series, this development was preceded by a concept of the multifractal spectrum by Halsey et al.[18] This has been applied to the analysis of the dissipation field in incompressible turbulence in Ref. 3. The basic idea is that along a time series there is a distribution of scaling laws whereby the p_m of Eq. (1) behave as $p_m \propto \varepsilon^{\alpha}$ and that the α behave with a probability distribution proportional to $\varepsilon^{-f(\alpha)}$. The function f then acts as a fractal dimension corresponding to a value α found along the time series. Insofar as the author can see, this is a postulate to be tested for real-time series. It is stated in Ref. 18 that it is hoped "to encourage experiments along these lines." In any event, the technique has been explored for the traces of Figs. 1a and 1b to test the utility of the method.

For a full development of the theory the reader is referred to Ref. 18. However, $f(\alpha)$ and α are related to the generalized dimension q, introduced earlier. If one can compute D_q from Eq. (1), the following two formulas allow construction of the $f(\alpha)$ vs α curve:

$$D_q = \{q\alpha(q) - f[\alpha(q)]\}/(q-1) \tag{2}$$

$$\alpha = \frac{\mathrm{d}}{\mathrm{d}q}[(q-1)D_q] \tag{3}$$

However, in the author's view there are two critical assumptions made in the derivation. First, it is assumed in a method of steepest descent that $q\alpha - f$ is "sufficiently" small, whereas the probability distribution for α contains no "holes" (null values). Second, it is assumed that f is everywhere concave when viewed from low α. No such presumptions are made in the multifractal pdf introduced earlier. It is a consequence of the theory that the maximum of the f-α curve gives $f_{\max} = D_0$, so that there will nowhere appear a local fractal dimension greater than D_0.

It will be noted that the computation of Eq. (1) must proceed by calculation of probabilities, and none of the approximations used in calculation of D_0 will work. For $q \leqq 0$ small p_m will yield large contributions to the sum, and, moreover, small numbers of points in a box yield a great statistical uncertainty in the calculation of p_m. That is, on rarefied portions of the time series are made the largest contributions to the generalized dimension for negative q. The opposite is true for positive q. These facts pose a computational difficulty for a single-valued digitized data time series as ε is varied. It matters not whether the data are digitized at fixed time intervals or at random time intervals (if the randomness is not tied to the physics of interest). There will come a point for negative q at small enough ε that the data cannot be believed. Finally, at small enough ε, p_m will be zero, which will not work for $q \leqq 0$.

An opposite problem occurs for large positive q. The dominant contribution to D_q for positive q is on regions of the curve densely populated by points. This causes problems at large ε, where an increase in ε by a factor of 2, say, tends to increase p_m by a factor of four for a given box because the whole graph is dense. On the other hand, at low ε the best answers are obtained because only a few boxes are densely populated and contribute to the sum of Eq. (1). Consequently, one has to look for the generalized dimension at high negative q at relatively high ε and for high positive q at relatively low ε. The D_q is still obtained from straight lines on

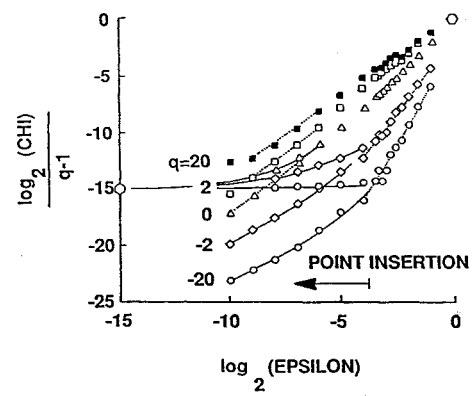

Fig. 7 Computations required for calculation of the generalized dimension of order q. Chi is the probability sum of Eq. (1). The straight lines are drawn in the regions of highest confidence for dimension determination for the various q. The solid curved lines show the asymptotic values obtained for negative and zero q if boxes are omitted when no points are found in a box located between the lower and upper bounds of y for a given t_i and ε. The data points to the left of the "point insertion" arrow indicate the results for negative q when points are added to a null box by taking points from another box.

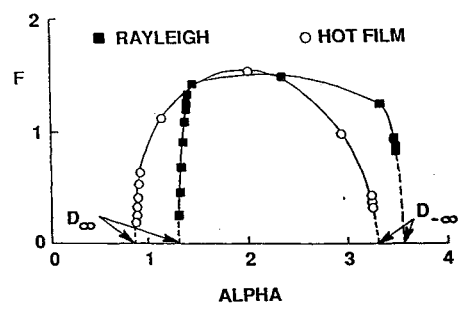

Fig. 8 The multifractal spectrum f-α curve for the hot film and Rayleigh data.

a log-log plot. This is illustrated in Fig. 7 for 16,384 points of the Rayleigh trace of Fig. 1b (where only 4096 points are shown). Clearly, some judgment must be applied.

This analysis has also been applied to the data of Fig. 1a. Applying Eqs. (2) and (3) to the obtained D_q values, the f-α plots of Fig. 8 result. For both curves, within experimental error, the maxima indeed correspond to D_0. The intercepts with the α axis would correspond to D_∞ on the left and $D_{-\infty}$ on the right. That is, in both rarefied and compact regions of the time series, the implication is that the fractal dimension is zero. This is counter to the revelations given earlier by the multifractal pdf. Moreover, there is no real structural difference in the two f-α curves to give an indication of a visual difference between the two data traces. This is believed to arise because of some of the aforementioned assumptions concerning the derivation of the method. Although the Rayleigh trace seems to be richer in high α content, this may be an artifact of some numerical error [note that a numerical derivative must be taken in Eq. (3)]. Finally, for a real fractal on a two-dimensional piece of paper (a Henón map or a Poincaré section of a multidimensional motion, for example), the separation between points in *both* vertical and horizontal directions has a connection with the real fractal properties of the figure. In the case of a time series digitized at fixed time intervals or at intervals not connected with the physics, the lateral spacing has nothing to do with the fractal-like properties of the figure. Consequently, the α scaling is distorted in one of the dimensions.

The conclusion of the author is that, although the multifractal spectrum may give some insight into true fractals (recall here that the time series are only fractal-like between an upper and a lower time scale), there is little to be gained with this analysis in turbulent combustion data series. Moreover, the computation involved is time-consuming. It is acknowledged that this conclusion may be somewhat controversial.

Fractal Interpolation

A serious question concerning statistical accuracy arises in many experiments that provide a sparse number of data points in a time series. This situation may arise, for example, because of expense or hazard in long run times or a slow repetition rate of, say, a pulsed laser. Two problems are involved: 1) the problem of obtaining correlation of neighboring points and 2) the problem of obtaining a reliable, statistically accurate pdf. Addressing the second point first, the following question is asked: Is it possible to augment the obtained data by an appropriate interpolation scheme, which retains physics and yields more accurate pdf information so that moments of the pdf can be believed?

Typically in turbulence one is interested in no more than a fourth moment of a pdf. But even at the second moment (variance or covariance), much less at a fourth moment (kurtosis or fourth-order correlation), tails on the pdf, near-zero value of the probability, statistical uncertainty is large and noise may be dominant. However, at high moments, these tails contribute significantly to the answer. It would be nice if a method of at least decreasing the statistical uncertainty were available by increasing the number of available

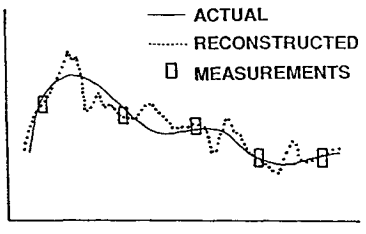

Fig. 9 Schematic of fractal reconstruction of data, given sparsely separated data points.

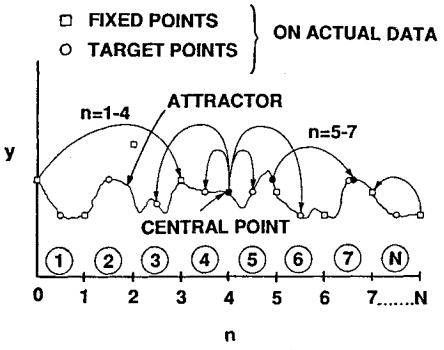

Fig. 10 Description of how the fractal interpolation scheme works and the strategy used to determine the unknown coefficients in the affine maps.

data points near these tails. Fortunately, there does appear a method, based upon fractal geometry, to accomplish this goal.

Consider the situation of Fig. 9 where certain data points are known, but they are too sparsely separated to clearly define the true experimental curve. If it is known that the curve is fractal-like over some range of time scales, it appears that an interpolation between points by a fractal would be superior to, for example, connecting the data points by straight lines. Fortunately, there is now a technique that allows a rational interpolation by fractals that, by the way, contains a straight-line interpolation as a special case (it is known as the "condensation set" of the fractal).[19,20]

There are many ways to implement the procedure, and the one to be presented is only one way. It was the method found by the author on the first try, but other methods may be invented by other workers. The strategy is shown in Fig. 10. Given a time series, divide it up into N (even) intervals, the interval number being denoted by n. To each endpoint of the interval there is a data point (that assumes equidistant time spacing of data points) through which it is demanded that the fractal curve fit will pass. At the midpoint of each interval there is also assumed a data point through which the curve will pass, but these points are called "target points." The target points will determine some parameters of the fitting procedure.

Assume, for the moment, that the algorithm in Eqs. (4) will converge to a line on a piece of paper that passes through all data points. Say that one is in interval n, and a random number generator has picked a new n with uniform probability over the interval $0-N$. Associated with the old n is y_{old} and t_{old}; a new y and new t are generated by the following affine (linear) relation:

$$t_{\text{new}} = t_{n-1} + (t_n - t_{n-1})(t_{\text{old}} - t_0)/(t_N - t_0) \tag{4a}$$

$$y_{\text{new}} = b_n(t_{\text{old}} - t_0) + C_n(y_{\text{old}} - y_0) + y_{n-1} \tag{4b}$$

with

$$b_n = [y_n - y_{n-1} - C_n(y_N - y_0)]/(x_N - x_0)$$

The N values of the constants C_n are free parameters that are to be chosen. Provided[19,20] $\Sigma_n|C_n| > 1$ and for all n $|C_n| < 1$ (the transformation, or map, is contractive), the procedure will generate a continuous (but not necessarily differentiable), unique fractal curve passing through all y_n,t_n points, where these have been chosen as data points at the interval endpoints. This procedure still does not guarantee passage through the target points; a choice of the C_n is required to do this.

The t transformation of Eqs. (4) takes an old t and moves it to interval n the same fraction of distance from the left endpoint of interval n to the right point of interval n as t was

from $n = 0$ to $n = N$. Consequently, if the central data point is designated as special, as it is in Fig. 10, it will always map to the central point of any chosen interval n. Then choose the C_n so that the y map of Eqs. (4) always maps $y_{N/2}$ into each target point for each n. One then has a fractal curve (called an "attractor" of the map), that hits all data points. The fractal dimension of the curve may be estimated by the implicit formula[19]

$$\sum_n |C_n|(t_n - t_{n-1})^{D_0 - 1} = 1 \tag{5}$$

Under this procedure the formula for the determination of C_n is

$$C_n = \frac{y_t - \frac{1}{2}(y_n + y_{n-1})}{y_{N/2} - \frac{1}{2}(y_n + y_0)} \tag{6}$$

If the map is contractive, the fractal dimension may then be determined by Eq. (5). A problem is that the C may not all have magnitude less than unity with this procedure. They will if the y values of the endpoints $n = 0$ and $n = N$ are high (low) enough while the midpoint at $n = N/2$ is low (high) enough so that the denominator of Eq. (6) has a magnitude that is sufficiently high. This requires careful selection of the data trace by the practitioner, and the data may be sufficiently sparse that this freedom is not available.

The aforementioned procedure has been applied to the data trace of Fig. 1b. First, 4096 data points were decimated to 512 data points, because good definition of the curve still resulted. More precisely, even with this decimation, neighboring points are highly correlated. This 512-point trace was then taken as the data trace "standard" against which all approximations are to be tested. Shown in Table 1 on the first line are the various statistical moments of this actual trace. In this case ρ is the autocorrelation coefficient at zero time delay, which is obviously unity. In other cases to be investigated ρ is the cross-correlation coefficient at zero time delay of the approximate curve against the standard, exact curve. The nearness to unity is a measure of the accuracy of the data fit. The nearness of the various statistical moments of the approximations compared with those of the exact curve are of more engineering use. That is, although it would be nice to hit the standard curve exactly, there are reasons why this cannot be expected, but the useful information (the moments) can be reproduced.

The results of Table 1 are rather remarkable. If one only had one-fourth of the real data, all of the statistical moments are badly estimated by direct computation. The estimates become even worse through two further decimations by a factor of two. The fractal fit for 128 data points is shown in the upper curve of Fig. 11. The fractal dimension computed by Eq. (5) is 1.45, close to the dimension calculated from many more points. From Table 1 it is seen that a remarkable improvement in the moments is achieved, compared with the raw truncated data. Also shown in Table 1 is the result obtained using a straight-line fit between each of the 128 data points (this may be generated from the condensation set by

Table 1 Fractal analysis of Rayleigh data

	No. of points	$\sigma^2 \times 10^{-6}$	$s/\sigma^{1.5}$	k/σ^2	ρ
Full data	512	2.74	1.84	9.52	1.
Truncated data	128	3.31	2.66	15.3	——
Fractal fit	128	2.78	1.81	9.54	.96
Straight line	128	2.35	1.99	11.5	.93
Truncated data	64	6.15	3.24	15.4	——
Fractal fit	64	3.18	2.16	10.4	.92
Truncated data	32	6.15	3.23	15.4	——
Fractal fit	32	3.38	1.90	18.9	.71

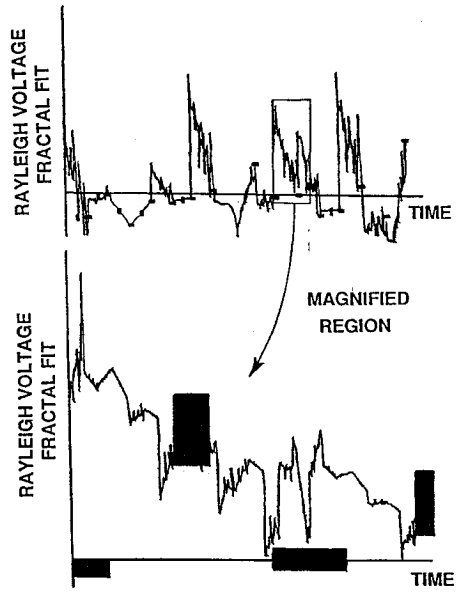

Fig. 11 Fractal interpolation results from the Rayleigh data decimated by a factor of four. The lower curve shows a magnified sector of the upper curve, illustrating the self-affine nature of the transformations.

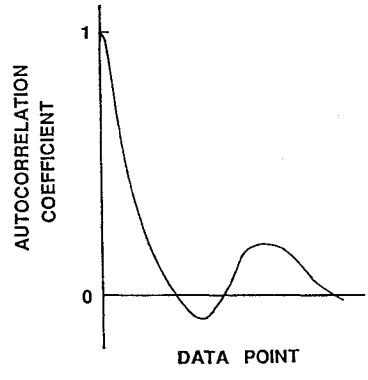

Fig. 12 Autocorrelation function of the Rayleigh data.

setting all C equal to zero or by direct straight-line fit). The straight-line method is highly inferior to the fractal fit. There is improvement of the statistical moments with the fractal fit at all decimations, compared with the truncated data, but the comparison with the exact moments becomes worse as the decimation increases.

The worth of the method depends highly on ρ. Unless ρ can be kept in the high 0.9 values, highly accurate results will not be obtained, although some improvement can still be gained by fractal fitting—*if neighboring data points have some correlation with each other*. The same procedure *does not work with the Raman data* of Fig. 1c precisely, as mentioned earlier, because adjacent data points are not correlated with each other. For the original data of Fig. 1b the autocorrelation coefficient, shown in Fig. 12, goes through the first zero crossing at a data point separation of 140 points, and there is a statistically significant correlation to about three times that value. For the 512-point data, therefore, the first zero crossing would take place at about 45 points and for the first truncation of Table 1 at about 11 points. Even for the 32-point data the zero crossing would take 3 points, with significant correlation out to 9 points.

The interpolation fractal produced is a self-affine curve, that reproduces itself (with rotation and contraction) on smaller and smaller scales. This can be seen upon magnification on the bottom half of Fig. 11. On the upper trace notice

the nearly straight-line segments that form a "V" on the left third of the trace. This can be seen as a (rotated, smaller) nearly inverted V on the magnified section. This behavior would repeat upon further magnification since the curve produced is really a self-affine fractal. The actual data curve is only fractal-like between an upper and lower time scale. But the picking of the data points ensures that the large scales are reproduced; the fractal interpolation ensures that the intermediate scales behave with proper fractal-like behavior; and the smaller scales are of little importance in the computation of statistical moments. The reason the method works is that it reproduces a roughness to the trace which increases the number (and, therefore statistical confidence) of points near the tail ends (and in the middle, for that matter) of the pdf.

It may be shown with standard statistical analysis techniques that, if the fitting curve, y_{fit}, consists of the true curve, y_{true}, plus a noise, v, where the noise is uncorrelated with the true curve, there is a bias introduced into an estimate of the variance of the fitted curve. That is,

$$\sigma^2_{\text{fit}} = \sigma^2_{\text{true}}(1+\varepsilon^2); \qquad \varepsilon^2 = (1-\rho^2)/\rho^2$$

This bias is highly sensitive to ρ. Notice in Table 1 that, as decimation is increased and ρ drops, the estimated variance increases over the true variance for the fractal fit.

It may also be shown, under the same assumption as that given earlier, that an estimate of the variance may be calculated by (under relatively weak assumptions)[21]

$$\text{Var}[\sigma^2_{\text{fit}}] = \frac{4}{N}\sum_{k=0}^{N}[R^2_{\text{true}}(k) + R^2_v(k)]$$

where R is the autocorrelation coefficient at a time delay of k data points, and now N is the number of fit points. What one is trading off is a larger number of data points against some noise. However, note that, when k is equal to the separation between data or data and target points, the noise is zero by construction, and this helps in accuracy.

Chaotic Dynamics

There is probably a deeper reason why the aforementioned procedure appears to work well. All of the data traces presented are really fairly simple insofar as chaos theory is concerned. That is, they are single-valued, aperiodic traces with a fairly low fractal dimension. According to Ref. 22, one should be able to model these traces with four to five delay equations in the form of iterative maps. That is, if a time delay τ between points is appropriately chosen,[23] it should be possible to reconstruct the *statistical properties* of the original curve by a set of equations of the form

$$v_1 = y_i = f_1(v_2, v_3, \ldots, v_z)$$
$$v_2 = y_{i-\tau} = f_2(v_2, v_3, \ldots, v_z)$$
$$v_3 = y_{i-2\tau} = f_3(v_2, v_3, \ldots, v_z)$$
$$\vdots$$
$$v_z = y_{i-(z-1)\tau} = f_z(v_2, v_3, \ldots, v_z)$$

with a clever choice of (nonlinear) f.

This view is reinforced when applying the procedure of Ref. 24 as a method of finding the minimum number of delay equations needed. Shown in Fig. 13 is a calculation of the eigenvalues of the covariance matrix of the data in Fig. 1b using 10 values of the time delay τ. Here τ is chosen as 50, although a better estimate of an appropriate time delay may have been obtained by the laborious computations introduced in Ref. 23. The number of eigenvalues off of the noise floor is an indicator of the number of delay equations, z, needed to produce an adequate chaotic dynamic for the data. Here the number indicated is five. Although there may be some limited forecasting ability of the generated analytical curve,[25] sensitivity to initial conditions will eventually destroy exact agreement. Nevertheless, the statistical properties of the experimental curve should be produced for all future times.[26] The creation of the necessary f is almost an art form and has not been attempted here. Nevertheless, in the cited references there is ample evidence that a procedure could be implemented to produce the desired result.

Hidden Variable Fractal Interpolation

There was a problem earlier with the fractal interpolation that all data sets would not produce a contractive mapping, contractivity being necessary for the attractor to be useful (and even exist). Moreover, the two-dimensional fractal graph is self-affine and upon magnification produces pictures at small time scales that are clearly not consistent with physics. There is a way out of these two problems (the first being the most important) by using hidden variable fractal interpolation.[27]

The method consists of adding a third dimension $u_i(t_i)$, and placing *any* (although some may be better than others) curve in this plane. Then, using the following affine maps for the t, y, and u and the same random jumping between intervals n, a curve in the y,t plane may be generated:

$$\begin{bmatrix} t \\ y \\ u \end{bmatrix}_{\text{new}} = \begin{bmatrix} a_n & 0 & 0 \\ c_n & d_n & h_n \\ k_n & l_n & m_n \end{bmatrix} \begin{bmatrix} t \\ y \\ u \end{bmatrix}_{\text{old}} + \begin{bmatrix} e_n \\ f_n \\ g_n \end{bmatrix}$$

All n-subscripted numbers in the 3×3 matrix must be chosen so that the map is contractive, and there are restrictions on all coefficients that are analogous to those used in the y-t map given earlier [Eqs. (4)]. However, there are many more free coefficients to be chosen by the practitioner to 1) produce any fractal dimension desired in the y-t plane and (more importantly) 2) make *any* data set with a *contractive* map, still going through all data and target points. That is, the aforementioned problem of some C_n having magnitude greater that unity can be avoided by choosing an appropriate background function, u. The resulting y-t plot need not be fractal and need not be self-affine.[27]

There is another potential use for the hidden variable technique in the construction of cross correlation between two physical quantities of interest, say, turbulent shear stress and heat transfer. Also say that one curve is well defined (as the Rayleigh trace) and the other is not well sampled (as the Raman trace). Yet presume there is a cross correlation between the two. If the well-sampled curve is placed in the background, u, and the sparse points of the poorly sampled curve is placed in the foreground, y, there is the possibility of

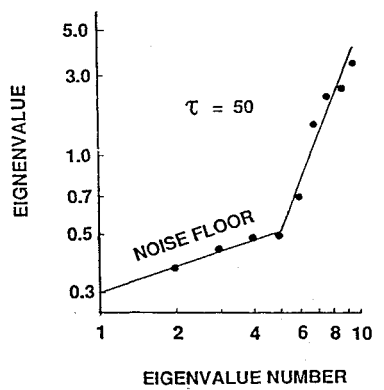

Fig. 13 Eigenvalues, in increasing size (by number encountered), of the covariance matrix of the time-delayed Rayleigh trace.

creating a better cross correlation, from a statistical sense, than from a sparse set of points, y_i. Work on the hidden variable technique will be reported upon in the future.

Conclusions

1) Many high-Reynolds-number turbulent combustion flows have physical quantity measurement time series with strong fractal-like properties. Quantification of the fractal properties yields new visual insight into the data and can indicate some new physical insight.

2) The distribution of fractal dimension in time along a time series can be used as a discriminator for nonlinear adaptive filtration, to remove unwanted noise from a signal while retaining much information usually removed by ordinary filtration even when adaptive and nonlinear.

3) The multifractal pdf introduced here appears to have superior properties in discrimination between different types of data traces compared with another type of multifractal analysis called the "multifractal spectrum." This conclusion is not general, but only applies to the type of time series investigated here with their digitization properties.

4) Fractal interpolation has been shown to be a valuable tool in increasing statistical confidence of moments of a data pdf when the data are sparse or the data record is short. The caveat is that neighboring data points must have some meaningful correlation with each other.

5) There appears a natural connection between fractal interpolation and chaotic dynamics whereby data may be reconstructed and extrapolated by nonlinear maps. Future work in this direction is warranted.

6) With the drawback of algebraic complexity there appear advantages in pursuing multiple variable fractal interpolation for both increasing flexibility in matching data and in constructing joint properties of data.

Acknowledgments

Michael F. Barnsley was my primary teacher in fractal geometry, and many of the ideas in this paper were a direct outgrowth of multiple discussions with him; his help (and patience) are gratefully acknowledged. Discussions with Ronald W. Schafer and Russell M. Mersereau were very helpful in developing the fractal filter. Discussions with John Elton on the multifractal spectrum were enlightening. Continuing discussions with Jechiel I. Jagoda have been highly useful on all aspects of the problem. The illustrations were prepared by Ronald E. Walterick. This work was sponsored by the Air Force Office of Scientific Research under Contract AFOSR-88-0001. Mitat Birkan is the contract monitor.

References

[1]Mandelbrot, B. B., *The Fractal Geometry of Nature*, Freeman, New York, 1983.

[2]Sreenivasan, K. R., and Meneveau, C., "The Fractal Facets of Turbulence," *Journal of Fluid Mechanics*, Vol. 173, 1986, pp. 357–386.

[3]Meneveau, C., and Sreenivasan, K. R., "The Multifractal Spectrum of the Dissipation Field in Turbulent Flows," *Physics of Chaos and Systems Far from Equilibrium*, edited by B. Nicols, North-Holland, Amsterdam, 1987.

[4]Gouldin, F. C., "An Application of Fractals to Modeling Premixed Turbulent Flames," *Combustion and Flame*, Vol. 68, 1987, pp. 249–266.

[5]Gouldin, F. C., Bray, K. N. C., and Chen, J.-Y., "Chemical Closure Model for Fractal Flamelets," Western States Section of the Combustion Institute Paper 88-37, 1988.

[6]Gouldin, F. C., "An Interpretation of Jet Mixing Using Fractals," Cornell University, Mechanical and Aerospace, Energy Program Rept. E-87-01, May 1987.

[7]Strahle, W. C., "Adaptive Nonlinear Filter Using Fractal Geometry," *Electronics Letters*, Vol. 24, Sept. 1988, pp. 1241–1248.

[8]Strahle, W. C., and Jagoda, J. I., "Fractal Geometry Applications in Turbulent Combustion Data Analysis," *23rd Symposium (International) on Combustion*, The Combustion Institute, Pittsburgh, PA, 1989.

[9]Barnsley, M. F., *Fractals Everywhere*, Academic, San Diego, CA, 1988.

[10]Walterick, R. E., deGroot, W. A., Jagoda, J. I., and Strahle, W. C., "Combustion Test Facility and Optical Instrumentation for Complex Turbulent Reacting Flow," AIAA Paper 88-0052, Jan. 1988.

[11]Libby, P. A., and Bray, K. N. C., "Countergradient Diffusion in Premixed Turbulent Flames," *AIAA Journal*, Vol. 19, Feb. 1981, pp. 205–213.

[12]Moon, F. C., *Chaotic Vibrations*, Wiley, New York, 1987, pp. 214–222.

[13]Barnsley, M. F., *Fractals Everywhere*, Academic, San Diego, CA, 1988, pp. 190–199.

[14]Hentschel, H. G. E., and Procaccia, I., "The Infinite Number of Generalized Dimensions of Fractals and Strange Attractors," *Physica*, Vol. 8, 1983, pp. 435–444.

[15]Rabiner, L. R., and Rader, C. M. (eds.), *Digital Signal Processing*, IEEE, New York, 1972, pp. 7–219.

[16]Tukey, J. W., *Exploratory Data Analysis*, Addison-Wesley, Reading, MA, 1977.

[17]Barnsley, M. F., and Jacquin, A., "Application of Recurrent IFS to Images," *STIE Proceedings of the Institute of Optical Engineering*, Vol. 1001, Pt. 1, Cambridge Univ. Press, Cambridge, UK, 1988, pp. 100–124.

[18]Halsey, T. C., Jensen, M. H., Kadanoff, L. P., Procaccia, I., and Shraiman, B. I., "Fractal Measures and Their Singularities: The Characterization of Strange Sets," *Physical Review A*, Vol. 33, Feb. 1986, pp. 1141–1151.

[19]Barnsley, M. F., "Fractal Functions and Interpolation," *Constructive Approximation*, Vol. 2, 1986, pp. 303–329.

[20]Barnsley, M. F., *Fractals Everywhere*, Academic, San Diego, CA, 1988, pp. 211–225.

[21]Bendat, J. S., and Piersol, A. G., *Random Data*, Wiley-Interscience, New York, 1971, pp. 175–176.

[22]Takens, F., "Detecting Strange Attractors in Fluid Turbulence," *Dynamical Systems and Turbulence*, edited by D. Rand and L. S. Young, Springer-Verlag, Berlin, 1981.

[23]Fraser, A. M., and Swinney, H. L., "Independent Coordinates for Strange Attractors from Mutual Information," *Physical Review A*, Vol. 33, Feb. 1986, pp. 1134–1140.

[24]Broomhead, D. S., and King, G. P., "Extracting Qualitative Dynamics from Experimental Data," *Physica*, Vol. 20, 1986, pp. 217–236.

[25]Farmer, J. D., and Sidorowich, J. J., "Exploiting Chaos to Predict the Future and Reduce Noise," *Evolution, Learning, and Cognition*, edited by Y. C. Lee, World Scientific, New York, 1988.

[26]Crutchfield, J. P., and McNamara, B. S., "Equations of Motion from a Data Series," *Complex Systems*, Vol. 1, 1987, pp. 417–432.

[27]Barnsley, M. F., *Fractals Everywhere*, Academic, San Diego, CA, 1988, pp. 234–239.